Modifying ring structures in lithium borate glasses under compression: MD simulations using a machine-learning potential

Shingo Urata [1,*] Aik Rui Tan [2] and Rafael Gómez-Bombarelli [2]

[1]*Innovative Technology Laboratories, AGC Inc., Yokohama, Kanagawa 230-0045, Japan*
[2]*Department of Materials Science and Engineering, Massachusetts Institute of Technology,
6-113, 77 Massachusetts Ave. Cambridge, Massachusetts 02139, USA*

Machine-learning potentials (MLPs) are advantageous in modeling boron coordination and three-membered rings (3-rings) in borate glasses. In this study, the prominent ability of MLP enables us to study how boron coordination varies during deformation, and the change in microstructure circumvents the overload stress in lithium borate and lithium borosilicate glasses via molecular dynamics simulations. Under uniaxial and triaxial compressive deformations, some of the threefold coordinated boron, ^{3}B, atoms were altered to be fourfold coordinated boron (^{4}B) at a strain range beyond elastic deformations. According to the local deformation analysis, a microstructure at around ^{4}B was determined to be rigid, specifically, that around ^{4}B forming a 3-ring exhibited the least flexibility. Conversely, the local region at around ^{3}B and oxygen atoms in nonring structures flexibly deformed following the entire deformation. As a result, nonbridging oxygen located in the vicinity of ^{3}B was found to migrate to form ^{4}B due to compression. Remarkably, most of the boron atoms became ^{4}B, and they formed abundant three membered rings in the borate glasses at a certain strain owing to the triaxial compression. Consequently, it is inferred that such a drastic structural variation can be the origin of high damage resistance of borate glasses.

I. INTRODUCTION

Boron is an essential element in improving the mechanical toughness of oxide glasses because a densification-induced structural variation of boron atoms from three (^{3}B) to fourfold (^{4}B) coordinated structures dissipates overloaded energy and circumvents the critical damage of brittle glass materials [1–6]. Analytical techniques, such as Raman scattering [1,6], inelastic x-ray scattering [2], and nuclear magnetic resonance (NMR) spectroscopy [3–5] are powerful technologies for observing structural alterations via *in-situ* experiments.

In addition to these experimental approaches, atomistic simulation is also a good alternative method for observing microstructure arrangements in any material. Specifically, molecular dynamics (MD) simulation is a well-established theoretical method for studying microstructure rearrangements by integrating dynamical atomic motions. Oxide glasses are usually studied using classical MD (CMD) simulations with analytical force fields because their inexpensive computation allows us to construct sufficiently large models to represent disordered microstructures of glasses [7]. Therefore, various analytical force fields have been developed to model multicomponent oxide glasses, for instance [8–12].

However, analytical force fields are limited in their ability to appropriately reproduce the coordination change of boron atoms from ^{3}B to ^{4}B because their structural variation nonlinearly relates to glass compositions, specifically,

amounts of alkaline ions [13–18]. This difficulty has been addressed by extending the analytical force fields to be composition-dependent. For instance, Kieu *et al.* defined the empirical correction functions to modify the partial charges and a parameter of the B-O pair potential as a function of [Na$_2$O]/[B$_2$O$_3$] and [SiO$_2$]/[B$_2$O$_3$] [19]. This force field was applied to measure the number of ^{4}B under an indenter by conducting nanoindentation simulations on sodium borosilicate glasses [20]. Du and Deng extended their Buckingham-type force field, Teter potential [9], by introducing a composition-dependent parameter to study sodium borosilicate glasses [21]. The practical transferability of the modified Teter potential to the other multicomponent borate glasses was also demonstrated [22]. Similarly, Urata *et al.* extended a force-matching potential [23,24] to study lithium borosilicate (LBS) glasses by defining a composition-dependent parameter [25].

These empirically extended analytical force fields can generate reasonable number of ^{3}B and ^{4}B atoms, consistent with experimental data. However, the two-body interatomic interaction models usually do not sufficiently form planar three-membered rings (3-rings) [26], which are called boroxol ring when all the boron atoms are ^{3}B. This intrinsic limitation of the analytical force fields prohibits the theoretical study on the mechanical response of borate glasses even though it is crucial in designing tougher glasses incorporating boron for industrial applications such as cover glasses of mobile devices [27] and coatings on an electrolyte and electrode in a solid battery [28]. *Ab initio* MD (AIMD) simulation is theoretically more accurate and reliable than CMD simulations. Indeed, it was demonstrated that AIMD simulations could

---

*Corresponding author: shingo.urata@agc.com

TABLE I. List of DFT data introduced to retrain the MLP.

Glass ID	Method	Condition	Data points
LBS-40-40-20	AIMD	melt-quench with T_{max} of 1500 K	~700
LBS-40-20-40	AIMD	melt-quench with T_{max} of 1500 K	~700
Li_2O	AIMD	$300 \sim 2300$ K every 500 K	250
Li_2O compress	DFT	$-0.01 \sim -0.4$ strain every 0.01	39
Li	AIMD	2000 K for 10 ps	100
O_2	AIMD	heating from 10 K to 300 K	46

reproduce reasonable ^3B / ^4B ratios and form 3-rings in three LBS glasses [26]. However, AIMD remains too expensive for studying various glasses and exploring an optimal glass composition.

Progressive advancements in machine-learning potentials (MLPs), which are typically trained to reproduce forces and energies of atoms calculated by the density functional theory (DFT), enable us to efficiently model materials with a comparable accuracy to AIMD simulations. In addition to crystalline oxides [29,30], MLPs were demonstrated to be applicable for modeling oxide glasses and their melts, such as silica glass [30–32], $MgSiO_3$ melt [33], borosilicate glasses [34], sodium borate glass [35], LBS glasses [36], and amorphous In_2O_3 [37].

In our previous study, the superior applicability of the MLP compared to the analytical force field [25] was verified by investigating the glass composition dependence of boron coordination and formation of the 3-rings in the LBS glasses [36]. However, the MLP constructed unsuitable over-coordinated silicon in some LBS glass models, which hindered further study on mechanical properties [36]. Therefore, this study first attempts to improve the accuracy of MLP in practically

obtaining fourfold coordinated silicon atoms by retraining the MLP with extra training datasets. Subsequently, MD simulations with an isothermal-isobaric ensemble (NPT) are conducted to verify its predictability on the density of lithium borate (LB) and LBS glasses because the NPT-MD simulation is essential for modeling experimentally unknown glasses. For further validation, short- and medium-range structures are compared to available experimental data. Ultimately, the effects of 3-rings and the structural alteration from ^3B to ^4B on the mechanical response of LB and LBS glasses are investigated.

II. COMPUTATIONAL METHODS

A. Machine-learning potential

To construct the MLP, DeepMD [38] was utilized in accordance with our previous research focused on borosilicate and LBS glasses [34,36]. DeepMD employs a local embedding network to generate rotationally and translationally invariant structural descriptors according to the distances between atom pairs. Subsequently, force and energy of atoms are evaluated via a multilayered fitting neural network. More details on the algorithm of DeepMD can be found in [38–40], and the hyperparameters were the same with our previous model [36].

The MLP was trained to reproduce force, energy, and virial, which were evaluated by the DFT calculations with the Perdew-Burke-Ernzerhof (PBE) [41] exchange-correlational functional for the generalized gradient approximation. The cutoff energy of the wave function was 600 eV. According to the energy/force conversion tests on three glass models, the cutoff energy was confirmed to be large enough to obtain reasonable energies and forces, as shown in Fig. S1 within the Supplemental Material (SM) [42]. All DFT calculations

TABLE II. LBS and LB glasses examined with approximately 300 atoms. Data for density and boron coordination of LBS were obtained from experimental database in Ref. [51]. Those of LB glasses were estimated from the approximation equations based on the experimental data taken from INTERGLAD (refer to Fig. S4 within the SM [42] and Ref. [36]).

| Glass ID	SiO_2	B_2O_3	Li_2O	K	R	Density (g/cm^3)	^3B	^4B
	(mol %)						(%)	
LBS-20-60-20	20	60	20	0.33	0.33	2.21	63.3	36.7
LBS-40-40-20	40	40	20	1.00	0.50	2.26	53.6	46.4
LBS-20-40-40	20	40	40	0.50	1.00	2.31	49.3	50.7
LBS-10-50-40	10	50	40	0.20	0.80	2.30	58.4	41.6
LBS-30-30-40	30	30	40	1.00	1.33	2.31	45.6	54.4
LBS-40-20-40	40	20	40	2.00	2.00	2.34	43.5	56.5
LBS-50-10-40	50	10	40	5.00	4.00	2.32	43.2	56.8
LBS-5-35-60	5	35	60	0.14	1.71	2.17	76.5	23.5
LBS-8-32-60	8	32	60	0.25	1.88	2.17	73.7	26.3
LBS-15-25-60	15	25	60	0.60	2.40	2.20	78.0	22.0
LBS-10-20-70	10	20	70	0.50	3.50	2.10	98.8	1.2
LB90	0	90	10	0.00	0.11	1.99	86.8	13.2
LB80	0	80	20	0.00	0.25	2.13	71.9	28.1
LB70	0	70	30	0.00	0.43	2.22	60.1	39.9
LB60	0	60	40	0.00	0.67	2.26	54.3	45.7
LB50	0	50	50	0.00	1.00	2.25	57.2	42.8
LB40	0	40	60	0.00	1.50	2.19	71.9	28.1
LB30	0	30	70	0.00	2.33	2.09	100.0	0.0
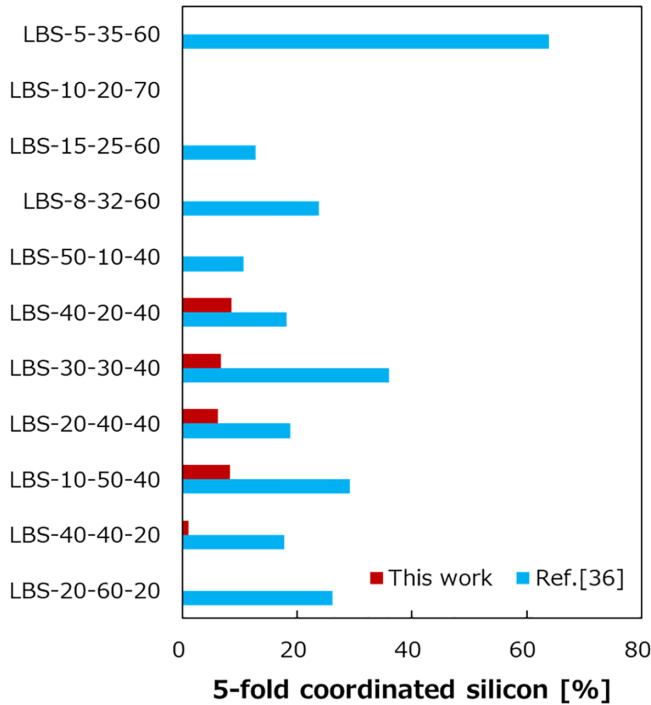
FIG. 1. Ratios of the fivefold coordinated silicon atoms formed in the LBS glass models comprising approximately 300 atoms. Dark red and cyan bars represent the results with the revised and previous MLPs [36], respectively.

were performed using the Vienna *Ab Initio* Package (VASP) [43,44]. The training datasets included the extra datasets in Table I and the 9749 datasets adopted in our previous study [36]. In the additional datasets, the configurations of $(SiO_2)_{40}(B_2O_3)_{40}(Li_2O)_{20}$ (LBS-40-40-20) and $(SiO_2)_{40}(B_2O_3)_{20}(Li_2O)_{40}$ (LBS-40-20-40) glasses were obtained by performing the melt-quench AIMD simulations. The LBS glass models were heated from 300 K to 1500 K at a heating rate of 1 K/fs, then equilibrated at 1500 K for 2 ps. The melt models were cooled down to 300 K at a cooling rate of

approximately 3 K/fs. The AIMD simulations of Li, O_2, and Li_2O were also conducted to add DFT data relating Li–Li and O–O interactions in addition to the DFT calculations on an uniaxially compressed Li_2O model down to –0.4 strain. These configurations were introduced to circumvent the unsuitable overlaps of these atoms, which were observed in our previous study [36]. In total, 11 650 configurations were prepared, as shown in Table S1 within the SM [42], and 10% of the data were used as test data.

B. Molecular dynamics simulations

The MLP-based MD (MLP-MD) simulations were conducted using the ASE package [45,46] with an NPT ensemble unlike the previous studies, which utilized a canonical ensemble, to verify its accuracy on the estimation of density. The atom motions were integrated with a 1-fs time step, and the temperature and pressure were controlled by a Nosé-Hoover thermostat [47] and Parinello-Rahman dynamics [48–50].

Table II presents a list of the LB and LBS glasses modeled with approximately 300 atoms, to verify its accuracies on density, silicon, and boron coordination. Then, the larger models comprising approximately 1000 atoms were constructed to investigate their medium-range structures and mechanical responses. The melt-quench simulations were conducted at 10- and 2-K/ps cooling rates to examine the cooling rate effect on the properties. To verify the reproducibility of the MLP-MD simulations, three independent models were constructed at a 2-K/ps cooling rate. After quenching, an NPT-MD simulation of 300 ps was performed to equilibrate the structures. The time variations of potential energy, kinetic energy, temperature, and density were monitored to ensure convergence. An example of this $[(SiO_2)_{10}(B_2O_3)_{50}(Li_2O)_{40}$ (LBS-10-50-40) glass models comprising 1000 atoms] is illustrated in Figs. S2(a)–S2(d) within the SM [42]. Furthermore, to assess energy convergence, MD simulations were conducted for 500 ps using a microcanonical (NVE) ensemble for three glass models: LBS-10-50-40 with 1000 atoms, $(B_2O_3)_{30}(Li_2O)_{70}$ (LB30) with 300 atoms, and $(B_2O_3)_{66.6}(Li_2O)_{33.3}$ (LB67) with 3000 atoms;

(a) Standard deviations of energy   (b) Standard deviations of force
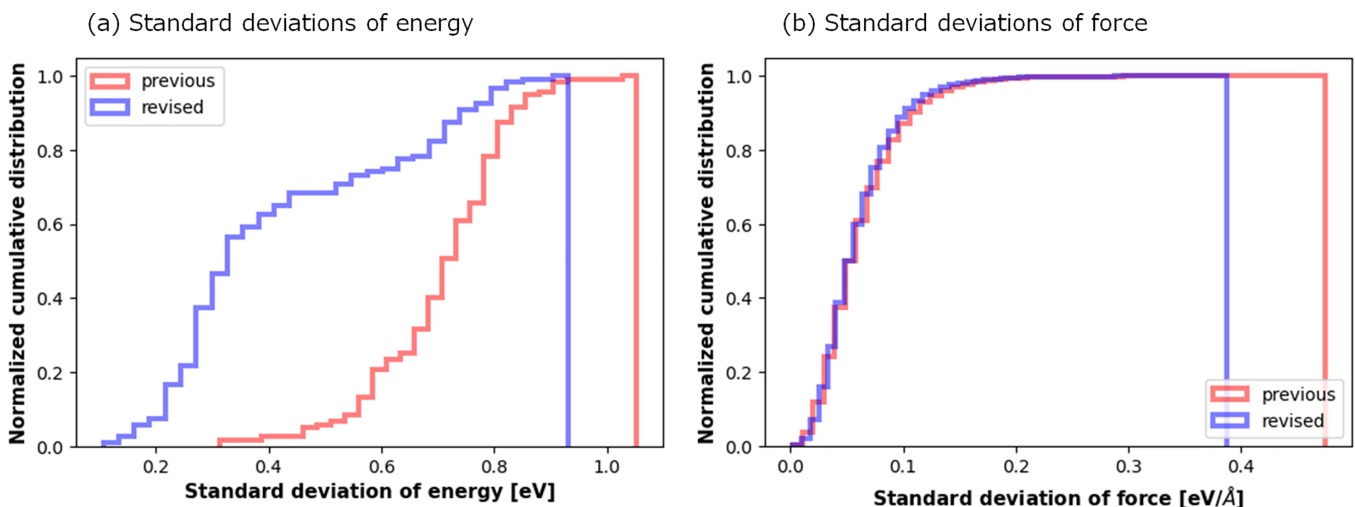

FIG. 2. Cumulative distributions of the standard deviations of estimated (a) energy and (b) force of $(SiO_2)_5(B_2O_3)_{35}(Li_2O)_{60}$ glass model.
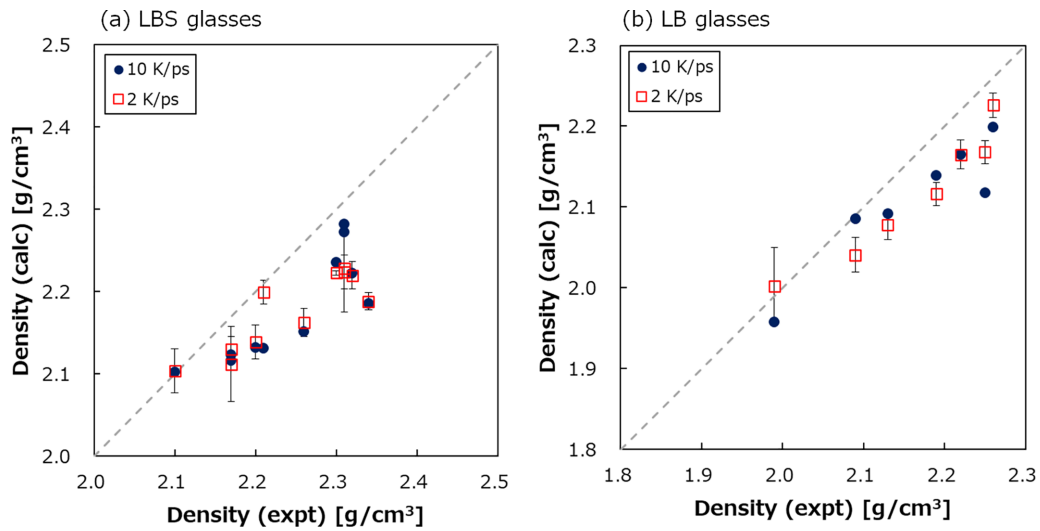
FIG. 3. Comparisons of density estimated using NPT-MD simulations with the MLP and experimental data for (a) LBS and (b) LB glasses comprising approximately 300 atoms.
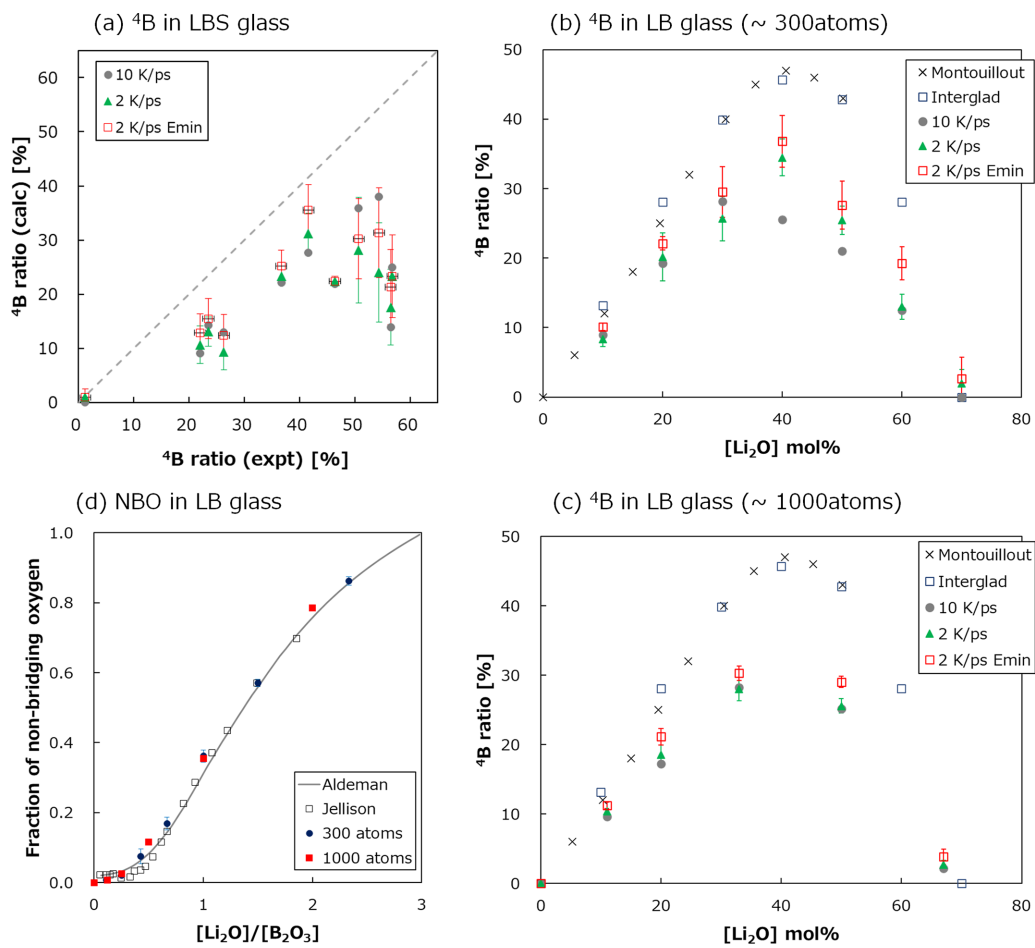

FIG. 4. Ratios of fourfold coordinated boron (^{4}B) in (a) the LBS glass models, (b) LB glass models with ∼300 atoms, and (c) ∼1000 atoms. In the legend, Montouillout [18] and Interglad denote experimental data, while simulation results are represented by the cooling rates, such as 10 K/ps and 2 K/ps. Emin indicates that the models were optimized by energy minimization after being equilibrated at 300 K. (d) Fraction of nonbridging oxygen in the LB glasses. The results of MLP-MD simulations correspond to the structures optimized by energy minimization after the melt-quench simulation at a cooling rate of 2 K/ps. Experimental data were taken from [56,57].
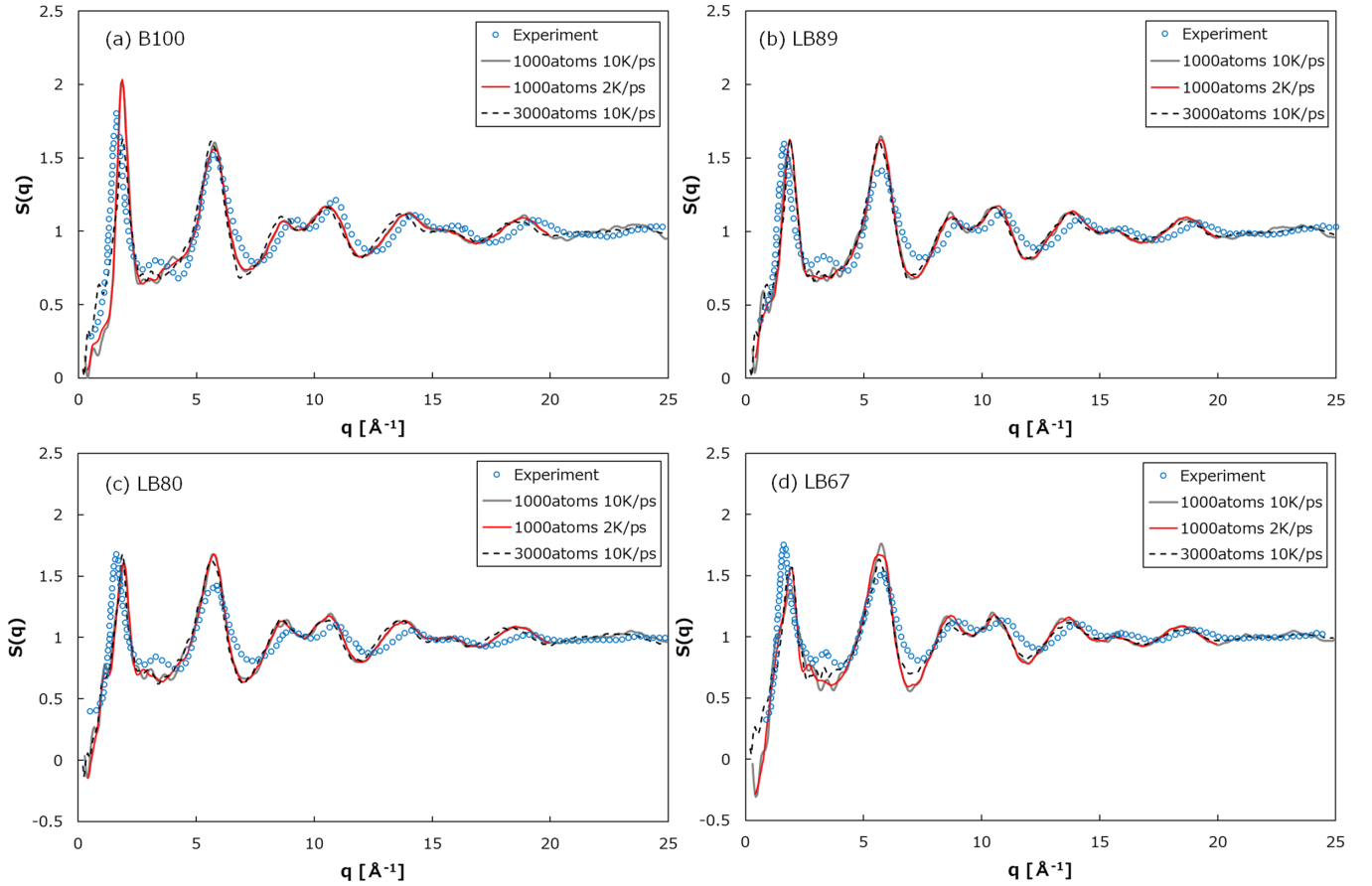
FIG. 5. Neutron structural factors S(q) of (a) B_2O_3 (B100), (b) $(B_2O_3)_{88.9}(Li_2O)_{11.1}$ (LB89), (c) $(B_2O_3)_{80}(Li_2O)_{20}$ (LB80), and (d) $(B_2O_3)_{66.7}(Li_2O)_{33.3}$ (LB67) glasses. The glass models composed of 1000 and 3000 atoms were constructed by the melt-quench simulations at cooling rates of 2 and 10 K/ps, respectively. The models with 1000 atoms were also obtained by the melt-quench simulations at cooling rates of 10 K/ps. The experimental data drawn by open circles are obtained from [58].

Figs. S2(e)–S2(g) within the SM [42]. These simulations were performed after the NPT-MD simulations for 300 ps at 300 K. As a result, sufficient convergence in the total energy was confirmed. Some of the final snapshots were visually shown in Fig. S3 within the SM [42].

It is to be noted that the initial configurations for MLP-MD simulations were obtained by conducting MD simulations using an analytical force field [25], to start the MLP-MD simulations with reasonable glass structures. The classical MD simulations were carried out in a canonical ensemble, starting from random configurations with assuming experimental density. The models were obtained by quenching from 3500 K to 300 K at a constant cooling rate of 1 K/ps, following a melting simulation at 3500 K.

III. SIMULATION RESULTS

A. Update MLP

To obtain the LBS glass models without the over-coordinated silicon atoms, the MLP was updated using the extra datasets presented in Table I. After 10^7 iterative training, the mean absolute errors (MAEs) of energy were 5.14×10^{-3} and 5.18×10^{-4} eV/atom for test and training data, respectively. The MEAs of force were 0.242 and 0.212 eV/Å for test

and training data, respectively. The MEA and maximum error (MXE) for each dataset are noted in Table S1 within the SM [42]. Via a trial and error process, it was determined that the fivefold coordinated silicon atoms were drastically decreased by learning the forces and energies of the configurations obtained by the AIMD simulations on LBS-40-40-20 and LBS-40-20-40, as illustrated in Fig. 1. This result indicates that the AIMD simulations provided more appropriate configurations for training the MLP than CMD simulations, which had been primarily utilized to obtain the glass configurations for calculating the DFT training datasets in our previous paper [36], although the CMD simulations also did not generate any fivefold coordinated silicon. The other training data were introduced to circumvent the undesired overlaps of atoms at high temperatures.

To understand how the updated MLP was improved, the uncertainties on force and energy were evaluated using extra DFT data on the configurations of the LBS-5-35-60 glass model comprising 299 atoms. This glass model was selected because the fivefold coordinated silicon was profoundly formed, as shown in Fig. 1. The configurations were extracted from the trajectories of the previous MLP-MD simulations for heating and quenching the model from 300 K to 1500 K and from 1000 K to 300 K, respectively. The quenching
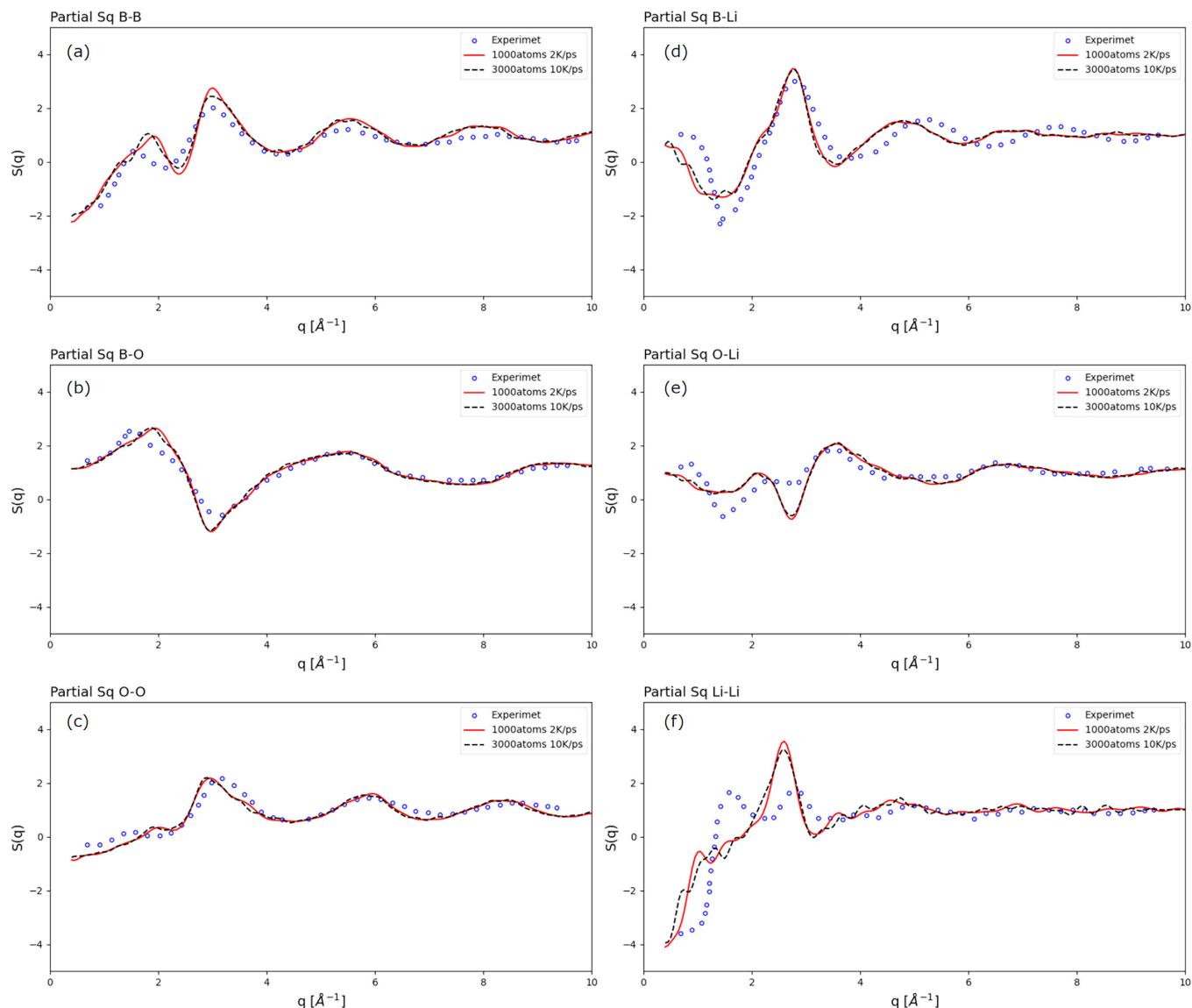
FIG. 6. Partial neutron structural factors of $(B_2O_3)_{66.7}(Li_2O)_{33.3}$ (LB67) glass. The experimental data drawn by open circles are obtained from [60]. The glass models composed of 1000 and 3000 atoms were constructed by the melt-quench simulations at cooling rates of 2 and 10 K/ps, respectively.

simulations were conducted for three cases by altering the retaining time at 1000 K. In total, 120 DFT datasets were prepared. The uncertainty was evaluated as a standard deviation of the values evaluated by five independent MLPs. These MLPs were trained using the same datasets, but the learning procedures commenced from different initial parameter sets. The ensemble method was employed because it is a robust metric for evaluating the uncertainty, as demonstrated in [32].

Consequently, both the previous and revised MLPs exhibit comparable accuracy on both energy and force, as shown in Fig. S5 within the SM [42]. However, the energy uncertainty of the revised MLP is significantly smaller than that of the previous MLP, as shown in Fig. 2. This implies that the MLP revised using the extra DFT datasets in Table I became more confident for estimating the energy of the LBS-5-35-60 model. The revised MLP also has shown lower force uncer-

tainty; however, the degree of improvement is less apparent than energy. Accordingly, it can be inferred that the uncertainty measured by the ensemble of multiple MLPs provides additional information to verify the reliability of the MLP, and the revised MLP was determined to be improved in this sense compared to the previous MLP.

B. Validation of MLP

Using the updated MLP, 11 LBS and 7 LB glasses comprising approximately 300 atoms were modeled by conducting the NPT-MD simulations. Figure 3 compares the densities obtained by the MLP-MD simulations with experimental data [36,51]. The MLP-MD simulations consistently underestimated the densities. This might be because DFT calculations often underestimate dispersion energy owing to a lack of electron correlation energy [52,53]. Nevertheless, the
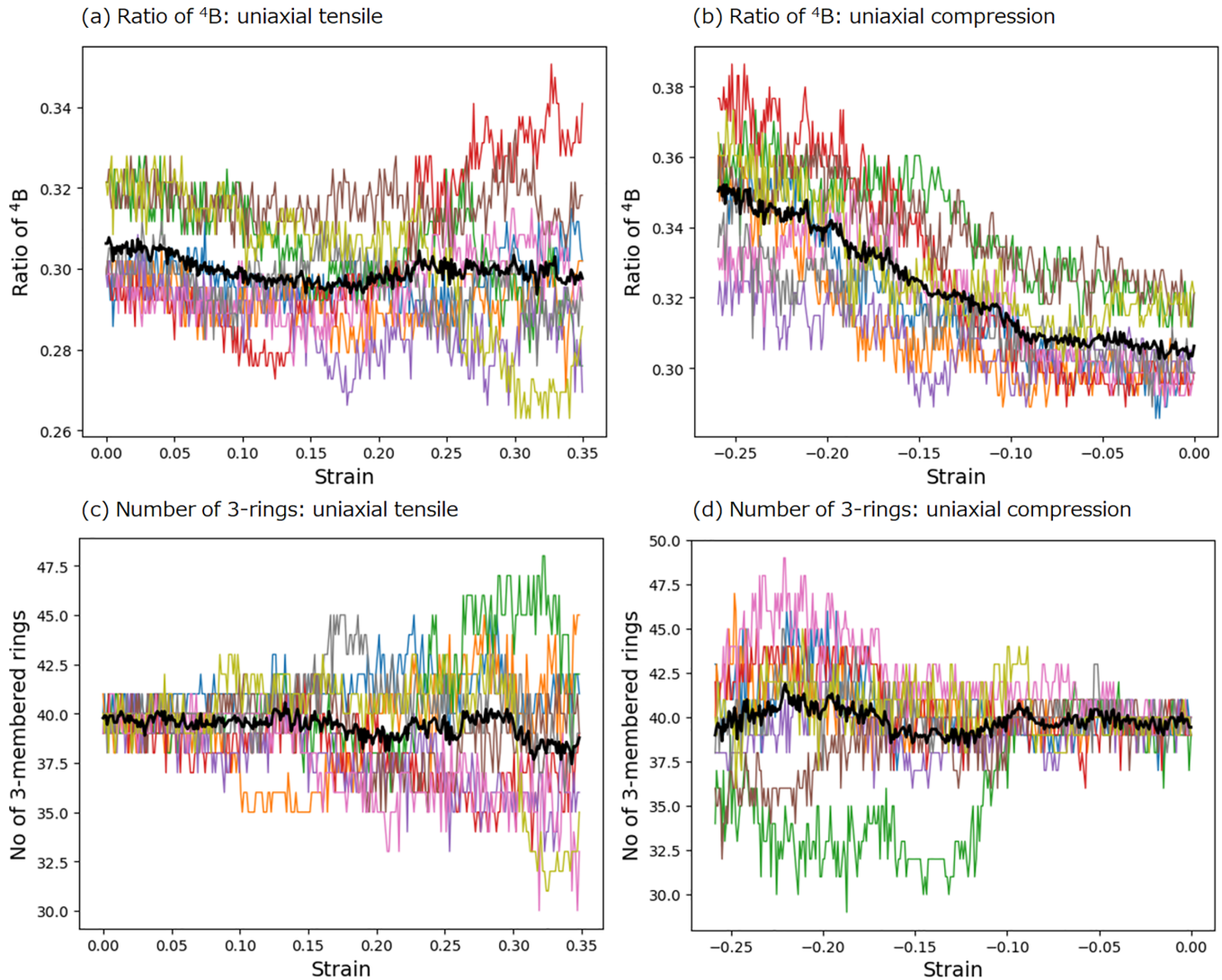
FIG. 7. Variations of ^{4}B ratio and number of three-membered rings during uniaxial tensile and compressive deformations of the LB67 models comprising 1000 atoms. Colored-thin lines are results of three directions of three independent models, respectively, and the black-bold lines represent the average of the nine simulations.

average deviations from the experimental data were only –0.069 and –0.050 g/cm^3 for the LBS and LB glasses, respectively, when the cooling rate was 2 K/ps, thereby indicating that the DFT data obtained by the PBE level of calculations are sufficiently accurate for the ionic oxides for which electrostatic interaction is dominant. The sufficient accuracy in density guarantees that the MLP-MD simulations are applicable to model the experimentally unknown LB and LBS glasses.

Figure 4 compares ^{3}B/^{4}B ratios obtained by the MLP-MD simulations and experimental data for the LBS and LB glasses. The simulation results agreed well with the experimental data of the LBS glasses whose ^{4}B ratio are less than 40%, whereas the LBS glasses possessing more ^{4}B were apparently underestimated. Similarly, for the LB glasses, the variation of ^{4}B ratio with the Li$_2$O content was qualitatively well reproduced, as illustrated in Figs. 4(b) and 4(c), while the maximum ^{4}B ratio at approximately Li$_2$O = 40 mol% was clearly underestimated. The glass models obtained with the

slower quenching rate possessed more ^{4}B. Furthermore, by conducting energy minimization after equilibrating the glass models at 300 K, both the LBS and LB glasses consistently increased ^{4}B. Therefore, it is expected that further slower quenching would develop more ^{4}B, although more computational resources or efficient algorithms [54,55] are necessary to obtain further relaxed structures even with the MLP, which is less demanding in computation than the AIMD simulations. In addition, the slightly but lower density obtained by the NPT-MD than experimental data is also responsible for the underestimation of the ^{4}B ratio.

For further validation, the fraction of nonbridging oxygen (NBO) in the LB glasses was compared to experimental data reported by Jellison *et al.* [56] and Alderman *et al.* [57], as shown in Fig. 4(d). Consequently, the NBO ratio estimated by the MLP-MD simulations agreed well with the experimental data within a practical accuracy in the entire composition range. In addition, no model size effect emerged on the NBO ratio. These results verify the sufficient accuracy of
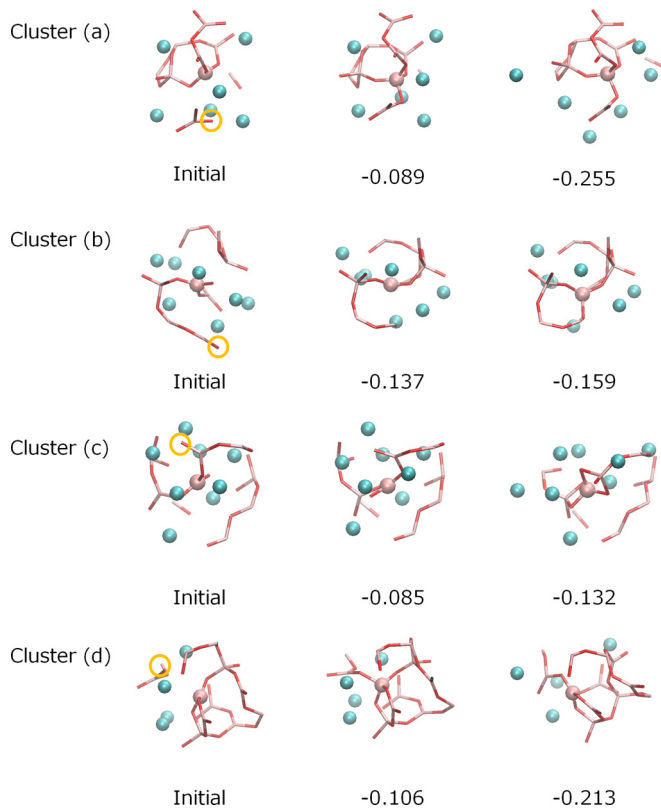
FIG. 8. Clusters extracted from the B67 glass models during uniaxial compressive deformation. The central boron, represented by a pink ball, varied its coordination from three to four. The surrounding atoms were initially located within a 4.5-Å distance from the central boron atoms. The numbers below the figures indicate the strain. Cyan balls represent lithium ions, while oxygen and boron atoms are shown in red and pink bonds, respectively. NBO atoms highlighted by orange circles eventually formed a new bond with the central ^{3}B atoms.

the MLP for modeling short-range structures of LBS and LB glasses.

Next, the accuracy in the medium-range structure was verified by analyzing neutron diffractions, S(q), of borate and three LB glasses, (B$_2$O$_3$) (B100), (B$_2$O$_3$)$_{88.9}$(Li$_2$O)$_{11.1}$ (LB89), (B$_2$O$_3$)$_{80}$(Li$_2$O)$_{20}$ (LB80), and LB67 by comparing to experimental data reported by Swenson *et al.* [58]. These models comprised approximately 1000 atoms. The simulation results were compared to experimental data, as illustrated in Fig. 5. The heights of the first sharp diffraction peaks (FPDS) were almost comparable with those of the experimental S(q), although the peak positions slightly shift toward a high q value. The second peaks of the models were slightly higher than experimental data, while their positions were comparable. In addition, the third and fourth peaks were almost consistent with the experimental profiles in their positions and heights. Consequently, the overall S(q) profiles were reproduced well by the MLP-MD simulations for all the LB glasses. These results verified that the MLP trained by DFT data can create practically accurate medium-range structures of the borate glasses.

In contrast, there is a clear discrepancy in a small peak at around 3-4 Å^{-1}. This peak is often referred to as the second principal peak [59]. To understand the reason for this difference, larger models comprising approximately 3000 atoms for B100, LB89, LB80, and LB67 glasses were constructed by conducting melt-quench simulations at a cooling rate of 10 K/ps. Their final snapshots are shown in Fig. S6 within the SM [42]. Furthermore, the partial structure factors of LB67 glass were compared with experimental data [60], as shown in Fig. 6. According to Fig. 5, the effect of model size is insubstantial, while the partial S(q) of O-Li, and Li-Li exhibit inconsistent peaks at around 2.5 Å^{-1} and that of B-Li shifts to smaller q value. These differences may be attributed to the discrepancy in the small principal peak of the overall S(q), implying that mixing of Li ions is somewhat different in the models obtained by MLP. However, these mismatches may not be crucial for studying the mechanical response primarily related to boron coordination because the good agreements with the experimental measurements in partial S(q) of B-B, B-O, and O-O assure that the glass network is reasonable.

C. Deformation simulations

1. Lithium borate glass

To understand how the microstructures comprising boron and its 3-rings vary the form during deformation, uniaxial tensile and compressive deformation simulations were performed at $\pm 1 \times 10^{-3}$ strain rates using the LB67 glass model with 1000 atoms, which possesses the most 3-rings, as shown in Fig. S7 within the SM [42]. Here, three directions in the three independent models obtained at a cooling rate of 2 K/ps were examined to verify the reproducibility, as shown in Fig. 7. In these figures, black bold lines represent values averaged over the nine simulations. In any case, both the ^{4}B ratio and the number of 3-rings were maintained until approximately ± 0.1 strain, which might relate to the range of elastic deformation, as observed in the stress-strain curves (refer to Fig. S8 within the SM [42]). Then, the numbers of structural units started to vary; however, some variations were not consistent among the nine simulations, specifically for the uniaxial tensile deformation. Conversely, the ^{4}B ratio consistently increased under uniaxial compression, implying that the boron increased the coordination of oxygen atoms to avoid unstable interaction between boron atoms in short range, and, thus, dissipate energy when the glass substrate is compressed.

To highlight the processes converting ^{3}B to ^{4}B during compressive deformation, four clusters were extracted from LB67 glass models, as shown in Fig. 8. In this figure, all the clusters were compressed vertically on the paper.

In the initial configuration of cluster (a), a ^{3}B atom in a four-membered ring is surrounded by a few lithium ions. Then, it transforms into ^{4}B at a strain of –0.089 by forming a new bond with an NBO atom located below it. Subsequently, the lithium ions are displaced away by the new B-O-B network. The additional bond remains until a strain of –0.255, indicating its sufficient stability. In cluster (b), an NBO atom located at the bottom gradually encircles and finally forms a bond with a central ^{3}B atom, resulting in the creation of a new four-membered ring. In cluster (c), a central ^{3}B atom is
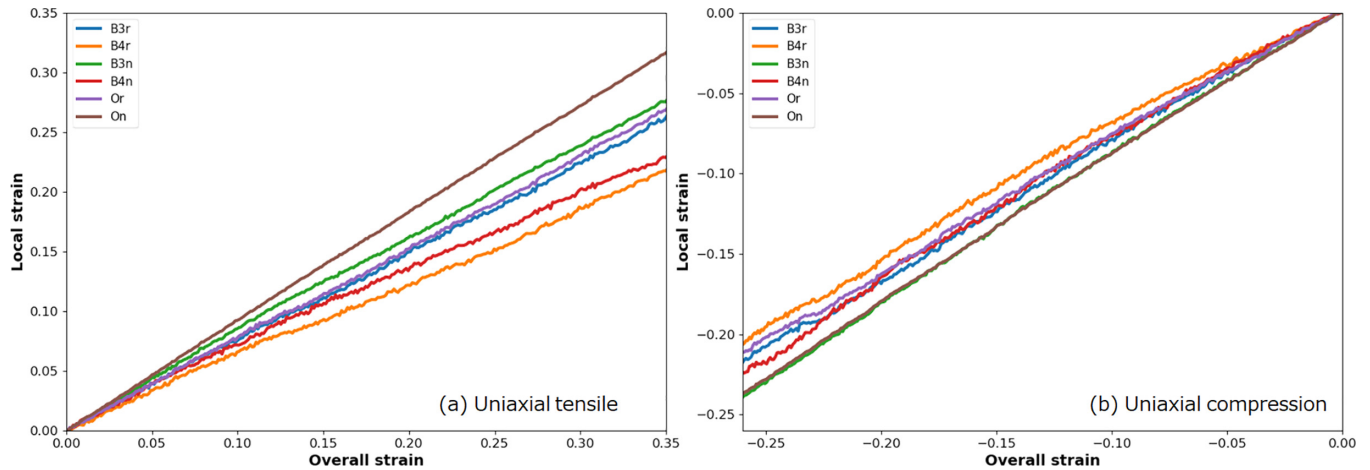
FIG. 9. Local deformations at each atom type in the LB67 glass model during uniaxial (a) tensile and (b) compressive deformations. Atoms were categorized into threefold coordinated boron in three-membered rings (B_{3r}) and nonring (B_{3n}), fourfold coordinated boron in three-membered rings (B_{4r}) and nonring (B_{4n}), and oxygen in three-membered rings (O_r) and nonring (O_n).

initially connected to another ^3B atom on the left. An NBO atom connected to the central ^3B atom gradually approaches the left ^3B atom, forming a small twofold ring with edge shar-

ing between the two boron atoms. Subsequently, another NBO above the central ^3B atom is displaced by compressive deformation, leading to additional coordination and the formation

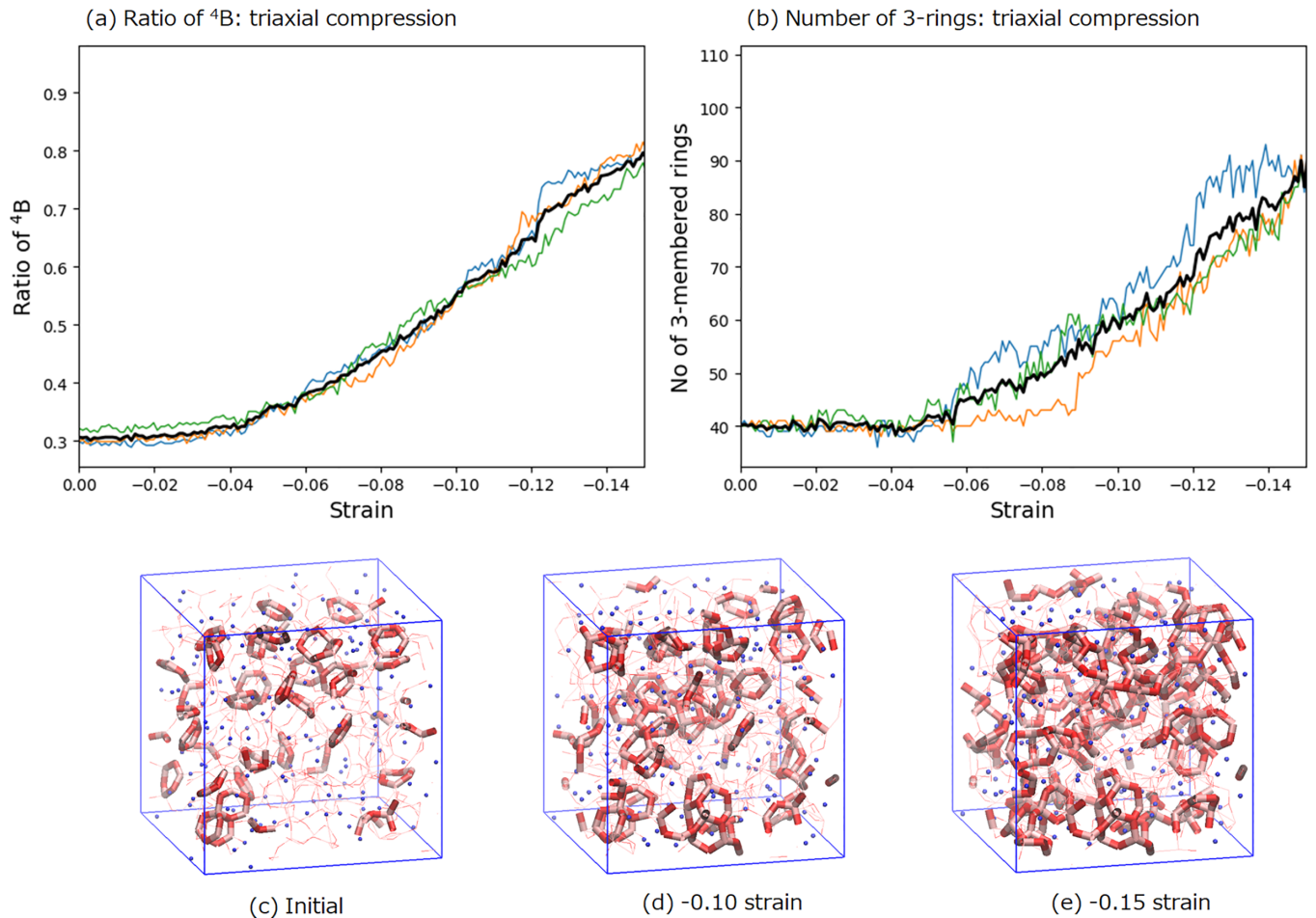

FIG. 10. Variations of (a) ^4B ratio and (b) number of three-membered rings during triaxial compression simulations of the LB67 models comprising 1000 atoms. Colored-thin lines represent results of three independent models, and the black-bold line is average of the three simulations. (c)–(e) Snapshots at 0, −0.1, and −0.15 strain of the triaxial compression simulations. Bold lines indicate three-membered rings, while thin lines represent B-O bonds. Lithium ions are presented as blue particles.

of ^{4}B. As a result, two sequential twofold rings, which would be unstable under normal conditions, appear under compression. In cluster (d), a central ^{3}B atom is part of a 3-ring. Interestingly, the 3-ring remains intact even when vertically compressed. In any case, additional bonds were formed with an NBO located close to the ^{3}B atoms, which were initially separated by several lithium ions. The compression caused the expulsion of lithium ions from the space between the two boron atoms. In other words, the high mobility of lithium ions and NBO atoms allowed to form an additional B-O-B network.

To compare the stabilities of ^{3}B and ^{4}B atoms in the compressed structures, the forces acting on boron atoms along the deformation direction were analyzed, as illustrated in Fig. S9 within the SM [42]. These histograms of absolute force values were evaluated using nine cases (three models × three directions). At any strain, the distributions and averages of forces for ^{3}B and ^{4}B atoms are almost the same, even though several ^{3}B atoms transformed into ^{4}B during deformation. This implies that the two forms exhibit comparable energy states, and it can be inferred that ^{3}B can transition to ^{4}B.

To observe how each atom type is affected by the uniaxial deformations, local deformation $\mathbf{F}_i$ at each atom i was analyzed using the following equations [61]:

$$\mathbf{M}_i = \sum_{j=1}^{N} \omega(|\mathbf{R}_{ij}|)\mathbf{R}_{ij} \otimes \mathbf{R}_{ij}, \qquad (1)$$

$$\mathbf{N}_i = \sum_{j=1}^{N} \omega(|\mathbf{R}_{ij}|)\mathbf{r}_{ij}(t) \otimes \mathbf{R}_{ij}, \qquad (2)$$

$$\mathbf{F}_i = \mathbf{N}_i \cdot \mathbf{M}_i^{-1}, \qquad (3)$$

where $\mathbf{R}_{ij} = \mathbf{R}_j - \mathbf{R}_i$ and $\mathbf{r}_{ij} = \mathbf{r}_j - \mathbf{r}_i$ represent positional vectors from an atom i to another atom j in the initial and current coordinations, respectively. ω is a localized positive window function represented by the Gaussian function, as

$$\omega(\mathbf{x}) = \frac{1}{(\pi h^2)^{3/2}}\exp\left(\frac{-\mathbf{x} \cdot \mathbf{x}}{h^2}\right) \qquad (4)$$

where h denotes the radius of the support, and we set it to 4.0 Å. In this support, lithium atoms were not considered because of their high diffusivity. According to $\mathbf{F}$, the local strain ϵ_{aa} is obtained as, $\epsilon_{aa} = F_{aa} - 1$ $(a = x, y, z)$.

The averaged local strain over the nine simulations is shown in Fig. 9. Here, the atom types were defined according to the initial configurations at zero strain. During both the uniaxial tensile and compressive simulations, the local strain at oxygen in the nonring structures (O_n) fairly follows the entire deformation, while that of oxygen in the 3-rings (O_r) is apparently smaller. Because O_r are all BO, while some of O_n are NBO, the latter is inferred to develop the more flexible microstructure. Following O_n, the ^{3}B in the nonring structures (B_{3n}) exhibited relatively large local strain, which implies that the ^{3}B in the chain-like structures were insubstantially constrained. In contrast, the local strain at ^{4}B comprising a 3-ring (B_{4r}) was minimum. Hence, it is expected that the highly coordinated boron atoms in the 3-rings makes the glass more rigid.

Comparing the tensile and compressive simulations, magnitude order of the local strain is slightly different. ^{4}B in the
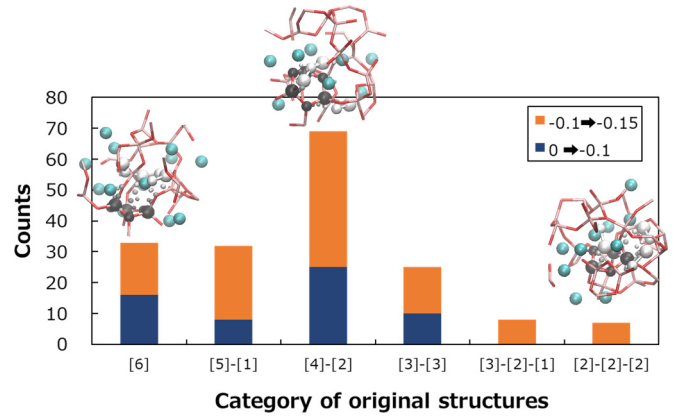

FIG. 11. The three-membered rings formed in LB67 glass under triaxial compression were categorized based on their initial structural units. The counts of 3-rings in vertical axis are sum of the three independent models. The labels on the horizontal axis represent the number of atoms in the structural units. The three inserted snapshots serve as examples: the left snapshot illustrates a 3-ring formed by sequentially connected six atoms, the middle snapshot shows a 3-ring formed by a pair of B-O-B-O and B-O bonds, and the right snapshot depicts a 3-ring formed by three B-O bonds coming together. In these snapshots, the large black and white particles represent the final and initial configurations of the 3-rings, respectively. The smaller particles between the white and black particles represent the trajectories of the atoms, with their colors becoming darker as the strain increases. Boron and oxygen atoms in the final configurations surrounding the 3-rings are represented by colored bonds, while lithium ions are depicted as cyan particles.

nonring structures (B_{4n}) exhibited smaller local strain than B_{4r} during stretching, whereas B_{4n} exhibited larger strain than B_3 in the 3-rings (B_{3r}) and O_r during compression. Therefore, it can be inferred that the connectivity of boron is mainly attributed to the rigidity of the LB-67 glass against tensile deformation, while the 3-rings resist the compressive deformation.

The structural changes in boron coordination and 3-rings formation are more evident when the LB67 glass models were isotropically compressed along tri-axis, as shown in Fig. 10. The ^{4}B ratio and number of 3-rings were almost constant until –0.05 strain, then both values monotonically increased when the model was compressed further. Notably, approximately 80% of the boron atoms turned to ^{4}B at –0.15 strain, and the increased connectivity generated abundant 3-rings at such high-pressure condition, as illustrated in Figs. 10(c)–10(e). These results imply that boron can avoid disruptive deformation by increasing the connectivity to form many 3-rings under triaxial compression, which might be a unique characteristic of boron to improve the damage resistance of glass products.

Figure 11 shows the categories of initial configurations that formed a 3-ring under triaxial compression, and some snapshots are inserted in this figure and additionally illustrated in Fig. S10 within the SM [42]. In the snapshots, the black particles represent atoms in a 3-ring, while the white particles represent their original configuration before compression. The other small particles between the white and black particles represent the positions of the atoms during compression, with their colors becoming darker as the strain increases, similar
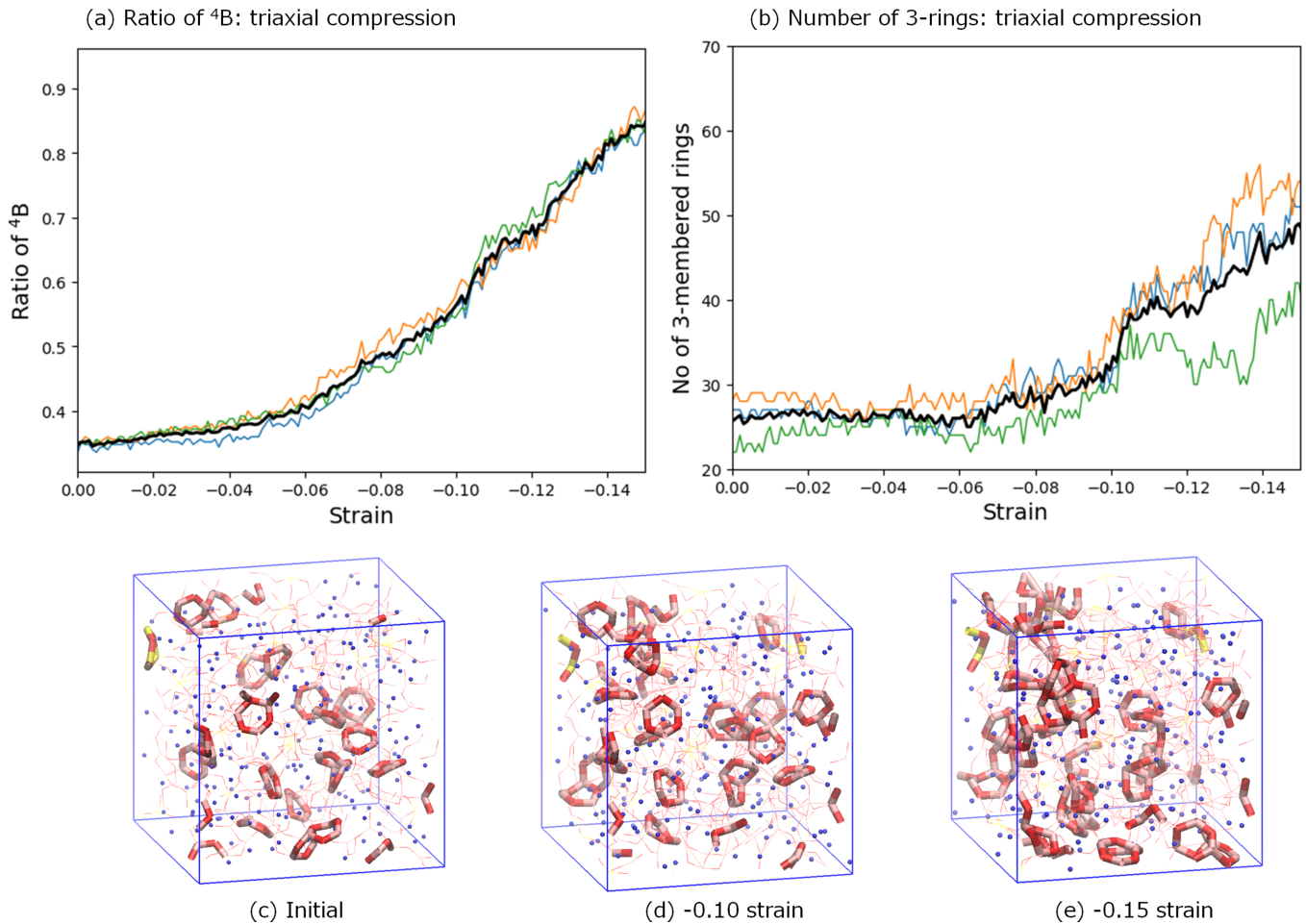
(a) Ratio of ^{4}B: triaxial compression

(b) Number of 3-rings: triaxial compression

(c) Initial   (d) -0.10 strain   (e) -0.15 strain

FIG. 12. Variations of (a) ^{4}B ratio and (b) number of three-membered rings during triaxial compression simulations of the LBS-10-50-40 models comprising 1000 atoms. Colored-thin lines represent results of three independent models, and the black-bold lines represent the average of the three simulations. (c)–(e) Snapshots at 0, –0.1, and –0.15 strain of the triaxial compression simulations. Bold lines depict three-membered rings, while thin lines are B-O and Si-O bonds. Lithium ions are presented as blue particles.

to time-colored coarse-grained particle trajectories [62]. Until a strain of –0.1, all the 3-rings created were composed of single or a pair of structural units. The 3-rings in Figs. S10(a)–S10(d) within the SM [42] were initially composed of sequentially connected six atoms (B-O-B-O-B-O), while those in Figs. S10(e)–S10(g) were formed by a B-O-B-O and a B-O bond. As the LB67 glass was further compressed, more diverse configurations, such as initially separated three B-O bonds, formed a 3-ring, as shown in Fig. S10(h) within the SM [42].

2. Lithium borosilicate glass

Next, the deformation simulations were conducted with the LBS-10-50-40 glass model comprising 1000 atoms. Three independent models were obtained by conducting the melt-quench simulations at a 2-K/ps cooling rate to verify the reproducibility of the simulation results. The variations in ^{4}B ratio and number of 3-rings during the uniaxial deformations are illustrated in Fig. S11 within the SM [42]. These results are analogous to the LB67 case (Fig. 7). Only the ^{4}B

ratio under compressive deformation demonstrated consistent variation among the nine simulations, and an increase in boron coordination beyond the elastic strain range (–0.05) was verified.

The same phenomena with the B67 glass model were observed in the variations of ^{4}B ratio and number of 3-rings during the triaxial deformation simulations, as summarized in Figs. 12(a) and 12(b). Indeed, most of the boron atoms became ^{4}B, and, consequently, 3-rings were abundant at the highly compressed conditions. Conversely, it should be highlighted that most of the 3-rings comprise only boron and oxygen atoms, as illustrated in Figs. 12(c)–12(e), even though a certain amount of silicon atoms were contained in the LBS-10-50-40 glass model. This result implies that boron exhibits a higher ability to form the small 3-rings to compensate compressive deformation more than silicon.

Figure 13 presents the local deformation around each atom type analyzed using Eqs. (1)–(3). The order of the stiffness at the location of the boron and oxygen types is consistent with that observed in the LB67 glass model. Notably, silicon atoms exhibit apparently lower local deformation compared
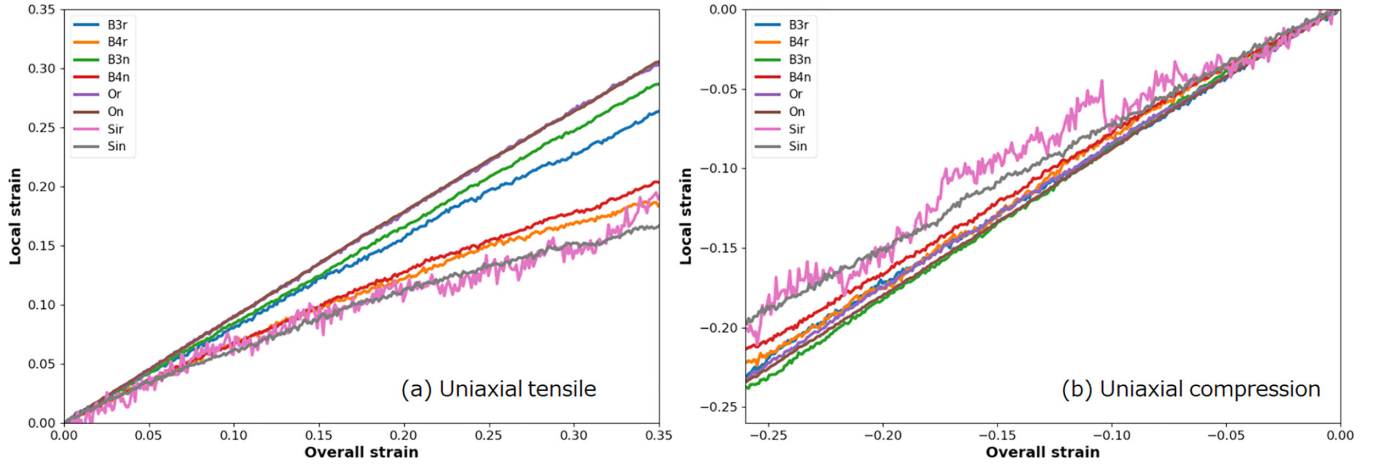
FIG. 13. Local deformations at each atom type in the LBS-10-50-40 glass model during uniaxial (a) tensile and (b) compressive deformations. Atoms were categorized into threefold coordinated boron in three-membered rings (B_{3r}) and nonring (B_{3n}), fourfold coordinated boron in three-membered rings (B_{4r}) and nonring (B_{4n}), oxygen in three-membered rings (O_r) and nonring (O_n), and silicon in three-membered rings (Si_r) and nonring (Si_n).

to boron and oxygen, regardless of whether the coordination site is in the 3-rings or not. It is thus conclusive that silicon brings locally stiff microstructures in alkaline borate glasses by forming the stable tetrahedral structural unit.

IV. CONCLUSIONS

To investigate mechanical responses of lithium borate and borosilicate glasses using MD simulations, the machine-learning potential developed in our previous study was updated to remedy its unphysical issue, which is an emergence of the over-coordinated silicon atoms, by adding the DFT datasets obtained by the AIMD simulations of two LBS glasses. After revising the MLP, the number of over-coordinated silicon was substantially suppressed, and the higher confidence of the revised MLP in evaluating energies than the previous MLP was verified by the ensemble-based method with the multiple MLPs.

The revised MLP exhibited practical accuracies in reproducing density, boron coordination, oxygen connectivity, and neutron diffraction patterns. Conversely, fourfold coordinated boron ratio was underestimated at the composition range where abundant ^{4}B atoms were observed by the experiments. Because the slower quenching and an additional energy minimization increased ^{4}B, it is expected that further slower quenching might obtain ^{4}B closer to experimental data, although it is computationally expensive.

Mechanical responses of $(B_2O_3)_{66.7}(Li_2O)_{33.3}$ and $(SiO_2)_{10}(B_2O_3)_{50}(Li_2O)_{40}$ glasses comprising approximately 1000 atoms were examined by performing uniaxial tensile, compressive, and triaxial compressive deformation simulations. During both the uniaxial tensile and compressive deformations, local deformation at the oxygen atoms in nonring structure almost perfectly matched the entire deformation, while an increase in boron coordination and 3-rings formations were determined to increase the local stiffness in the microstructures of the LB and LBS glasses. Consequently, the ^{4}B atoms in the 3-rings apparently demonstrated smaller local strain compared to the entire strain. Furthermore, in the LBS glass, silicon was found to be stiffer than any type of boron and oxygen atoms. Therefore, nonuniform deformation in nanoscale is inferred in the alkaline borate and borosilicate glasses.

Under uniaxial and triaxial compression, ^{4}B fraction increased when the glass models were compressed until the strain range where inelastic deformation is evoked. This observation ensured that the boron atoms increased the co-ordination number to avoid unfavorable interactions between each other by having an additional oxygen coordination under compressive deformation. Consequently, the ^{4}B fraction increased more when compressed further, thereby resulting in the formation of more 3-rings in the microstructures under triaxial compression. Remarkably, silicon atoms rarely contributed to form the 3-rings in the LBS glass even when substantially compressed, which implies a superior ability of boron in varying its form under such extreme condition for circumventing disruptive damages.

In summary, the prominent ability of boron to compensate a compressive deformation by increasing the oxygen coordination and forming 3-rings was demonstrated by the MLP-MD simulations, owing to its superior machine-learning potential in reproducing the practical microstructures comprising reasonable four-coordinated boron atoms and three-membered rings.

The DFT data, input file for using DeePMD, and the optimized potential are available at the Zenodo repository [63].

[1] M. Grimsditch, A. Polian, and A. C. Wright, Irreversible structural changes in vitreous B_2O_3 under pressure, Phys. Rev. B **54**, 152 (1996).

[2] S. K. Lee, P. J. Eng, H.-K. Mao, Y. Meng, M. Newville, M. Y. Hu, and J. Shu, Probing of bonding changes in B_2O_3 glasses at high pressure with inelastic x-ray scattering, Nat. Mater. **4**, 851 (2005).

[3] J. Wu, J. Deubener, J. F. Stebbins, L. Grygarova, H. Behrens, L. Wondraczek, and Y. Yue, Structural response of a highly viscous aluminoborosilicate melt to isotropic and anisotropic compressions, J. Chem. Phys. **131**, 104504 (2009).

[4] L. Wondraczek, S. Sen, H. Behrens, and R. E. Youngman, Structure-energy map of alkali borosilicate glasses: Effects of pressure and temperature, Phys. Rev. B **76**, 014202 (2007).

[5] M. N. Svenson, T. K. Bechgaard, S. D. Fuglsang, R. H. Pedersen, A. Ø. Tjell, M. B. Østergaard, R. E. Youngman, J. C. Mauro, S. J. Rzoska, M. Bockowski *et al.*, Composition-structure-property relations of compressed borosilicate glasses, Phys. Rev. Appl. **2**, 024006 (2014).

[6] P. Malchow, K. Johanns, D. Möncke, S. Korte-Kerzel, L. Wondraczek, and K. Durst, Composition and cooling-rate dependence of plastic deformation, densification, and cracking in sodium borosilicate glasses during pyramidal indentation, J. Non-Cryst. Solids **419**, 97 (2015).

[7] A. Pedone, M. Bertani, L. Brugnoli, and A. Pallini, Interatomic potentials for oxide glasses: Past, present, and future, J. Non-Cryst. Solids: X **15**, 100115 (2022).

[8] A. Pedone, G. Malavasi, M. C. Menziani, A. N. Cormack, and U. Segre, A new self-consistent empirical interatomic potential model for oxides, silicates, and silica-based glasses, J. Phys. Chem. B **110**, 11780 (2006).

[9] J. Du and A. Cormack, The medium range structure of sodium silicate glasses: A molecular dynamics simulation, J. Non-Cryst. Solids **349**, 66 (2004).

[10] S. Sundararaman, L. Huang, S. Ispas, and W. Kob, New interaction potentials for borate glasses with mixed network formers, J. Chem. Phys. **152**, 104501 (2020).

[11] M. Bertani, A. Pallini, M. Cocchi, M. C. Menziani, and A. Pedone, A new self-consistent empirical potential model for multicomponent borate and borosilicate glasses, J. Am. Ceram. Soc. **105**, 7254 (2022).

[12] S. Urata and R. Kado, Effect of Al_2O_3 addition on the thermal expansion of sodium alkaline-earth silicate glasses: A molecular dynamics study, J. Am. Ceram. Soc. **106**, 1809 (2023).

[13] W. L. Konijnendijk and J. Stevels, The structure of borate glasses studied by raman scattering, J. Non-Cryst. Solids **18**, 307 (1975).

[14] Y. Yun and P. Bray, Nuclear magnetic resonance studies of the glasses in the system $Na_2O\ B_2O_3\ SiO_2$, J. Non-Cryst. Solids **27**, 363 (1978).

[15] J. Zhong, X. Wu, M. Liu, and P. Bray, Structural modeling of lithium borosilicate glasses via NMR studies, J. Non-Cryst. Solids **107**, 81 (1988).

[16] M. R. Chialanza, R. Keuchkerian, A. Cárdenas, A. Olivera, S. Vazquez, R. Faccio, J. Castiglioni, J. Schneider, and L. Fornaro, Correlation between structure, crystallization and thermally stimulated luminescence response of some borate glass and glass-ceramics, J. Non-Cryst. Solids **427**, 191 (2015).

[17] G. Lelong, L. Cormier, L. Hennet, F. Michel, J.-P. Rueff, J. M. Ablett, and G. Monaco, Lithium borate crystals and glasses: How similar are they? A non-resonant inelastic x-ray scattering study around the B and O *K*-edges, J. Non-Cryst. Solids **472**, 1 (2017).

[18] V. Montouillout, H. Fan, L. del Campo, S. Ory, A. Rakhmatullin, F. Fayon, and M. Malki, Ionic conductivity of lithium borate glasses and local structure probed by high resolution solid-sate NMR, J. Non-Cryst. Solids **484**, 57 (2018).

[19] L.-H. Kieu, J.-M. Delaye, L. Cormier, and C. Stolz, Development of empirical potentials for sodium borosilicate glass systems, J. Non-Cryst. Solids **357**, 3313 (2011).

[20] D. Kilymis and J.-M. Delaye, Nanoindentation studies of simplified nuclear glasses using molecular dynamics, J. Non-Cryst. Solids **401**, 147 (2014).

[21] L. Deng and J. Du, Development of effective empirical potentials for molecular dynamics simulations of the structures and properties of boroaluminosilicate glasses, J. Non-Cryst. Solids **453**, 177 (2016).

[22] L. Deng and J. Du, Development of boron oxide potentials for computer simulations of multicomponent oxide glasses, J. Am. Ceram. Soc. **102**, 2482 (2019).

[23] S. Urata, N. Nakamura, K. Aiba, T. Tada, and H. Hosono, How fluorine minimizes density fluctuations of silica glass: Molecular dynamics study with machine-learning assisted force-matching potential, Mater. Des. **197**, 109210 (2021).

[24] S. Urata, N. Nakamura, T. Tada, and H. Hosono, Molecular dynamics study on the co-doping effect of Al_2O_3 and fluorine to reduce rayleigh scattering of silica glass, J. Am. Ceram. Soc. **104**, 5001 (2021).

[25] S. Urata, T. Miyajima, N. Kayaba, L. Deng, and J. Du, Development of a force field for modeling lithium borosilicate glasses, Int. J. Appl. Glass Sci. **13**, 444 (2022).

[26] T. Ohkubo, S. Urata, Y. Imamura, T. Taniguchi, N. Ishioka, M. Tanida, E. Tsuchida, L. Deng, and J. Du, Modeling the structure and dynamics of lithium borosilicate glasses with *ab initio* molecular dynamics simulations, J. Phys. Chem. C **125**, 8080 (2021).

[27] T. T. Fernandez, S. Gross, K. Privat, B. Johnston, and M. Withford, Designer glasses—Future of photonic device platforms, Adv. Funct. Mater. **32**, 2103103 (2022).

[28] E. Il'ina, E. Lyalin, T. Kuznetsova, and A. Pankratov, Cathode modification by Li_2O-B_2O_3-SiO_2 glass addition for all-solid-state battery creation, Ionics **28**, 3635 (2022).

[29] L. C. Erhard, J. Rohrer, K. Albe, and V. L. Deringer, A machine-learned interatomic potential for silica and its relation to empirical models, npj Comput. Mater. **8**, 90 (2022).

[30] K. Kobayashi, H. Nakamura, A. Yamaguchi, M. Itakura, M. Machida, and M. Okumura, Machine learning potentials for tobermorite minerals, Comput. Mater. Sci. **188**, 110173 (2021).

[31] I. Balyakin, S. Rempel, R. Ryltsev, and A. Rempel, Deep machine learning interatomic potential for liquid silica, Phys. Rev. E **102**, 052125 (2020).

[32] A. R. Tan, S. Urata, S. Goldman, J. C. Dietschreit, and R. Gómez-Bombarelli, Single-model uncertainty quantification in neural network potentials does not consistently outperform model ensembles, npj Comput Mater **9**, 225 (2023).

[33] J. Deng and L. Stixrude, Thermal conductivity of silicate liquid determined by machine learning potentials, Geophys. Res. Lett. **48**, e2021GL093806 (2021).

[34] S. Urata, N. Nakamura, T. Tada, A. R. Tan, R. Gómez-Bombarelli, and H. Hosono, Suppression of Rayleigh scattering in silica glass by codoping boron and fluorine: Molecular dynamics simulations with force-matching and neural network potentials, J. Phys. Chem. C **126**, 2264 (2022).

[35] T. Kato and S. Urata, Boron coordination and three-membered ring formation in sodium borate glasses: A machine-learning molecular dynamics study, J. Am. Ceramics Soc. **107**, 2888 (2023)..

[36] S. Urata, Modeling short-range and three-membered ring structures in lithium borosilicate glasses using a machine-learning potential, J. Phys. Chem. C **126**, 21507 (2022).

[37] S. Urata, N. Nakamura, J. Kim, and H. Hosono, Role of hydrogen-doping for compensating oxygen-defect in non-stoichiometric amorphous In_2O_{3-x}: modeling with a machine-learning potential, J. Appl. Phys. **134**, 115105 (2023).

[38] L. Zhang, J. Han, H. Wang, R. Car, and E. Weinan, Deep potential molecular dynamics: A scalable model with the accuracy of quantum mechanics, Phys. Rev. Lett. **120**, 143001 (2018).

[39] L. Zhang, J. Han, H. Wang, W. Saidi, R. Car, R. Car, and E. Weinan, End-to-end symmetry preserving inter-atomic potential energy model for finite and extended systems, in *32nd Conference on Neural Information Processing Systems (NeurIPS 2018), Montréal, Canada*, Vol. 31 (Neural Information Processing Systems Foundation, Inc., San Diego, CA, 2018), pp. 4441–4451.

[40] H. Wang, L. Zhang, J. Han, and E. Weinan, Deepmd-kit: A deep learning package for many-body potential energy representation and molecular dynamics, Comput. Phys. Commun. **228**, 178 (2018).

[41] J. P. Perdew, K. Burke, and M. Ernzerhof, Generalized gradient approximation made simple, Phys. Rev. Lett. **77**, 3865 (1996).

[42] See Supplemental Material at http://link.aps.org/supplemental/10.1103/PhysRevMaterials.8.033602 for additional details of the MD simulations, DFT calculations, MLP optimization, and snapshots of the structural models.

[43] G. Kresse and J. Furthmüller, Efficient iterative schemes for *ab initio* total-energy calculations using a plane-wave basis set, Phys. Rev. B **54**, 11169 (1996).

[44] G. Kresse and J. Furthmüller, Efficiency of *ab-initio* total energy calculations for metals and semiconductors using a plane-wave basis set, Comput. Mater. Sci. **6**, 15 (1996).

[45] S. R. Bahn and K. W. Jacobsen, An object-oriented scripting interface to a legacy electronic structure code, Comput. Sci. Eng. **4**, 56 (2002).

[46] A. H. Larsen, J. J. Mortensen, J. Blomqvist, I. E. Castelli, R. Christensen, M. Dułak, J. Friis, M. N. Groves, B. Hammer, C. Hargus *et al.*, The atomic simulation environment—A python library for working with atoms, J. Phys.: Condens. Matter **29**, 273002 (2017).

[47] S. Nosé, A unified formulation of the constant temperature molecular dynamics methods, J. Chem. Phys. **81**, 511 (1984).

[48] B. L. Holian, A. J. De Groot, W. G. Hoover, and C. G. Hoover, Time-reversible equilibrium and nonequilibrium isothermal-isobaric simulations with centered-difference Stoermer algorithms, Phys. Rev. A **41**, 4552 (1990).

[49] S. Melchionna, G. Ciccotti, and B. Lee Holian, Hoover NPT dynamics for systems varying in shape and size, Mol. Phys. **78**, 533 (1993).

[50] S. Melchionna, Constrained systems and statistical distribution, Phys. Rev. E **61**, 6165 (2000).

[51] N. Tsuda, M. Tanida, and T. Miyajima, Development of Li+ conducting glass materials, AGC Research Report **68**, 8 (2018).

[52] S. Tsuzuki, T. Uchimaru, M. Mikami, and S. Urata, Ab initio calculations of intermolecular interaction of CHF_3 dimer: Origin of attraction and magnitude of CH/F interaction, J. Phys. Chem. A **107**, 7962 (2003).

[53] S. Urata, S. Tsuzuki, A. Takada, M. Mikami, T. Uchimaru, and A. Sekiya, Analysis of the intermolecular interactions between CH_3OCH_3, CF_3OCH_3, CF_3OCF_3, and CH_2F_2, CHF_3, J. Comput. Chem. **25**, 447 (2004).

[54] S. Urata, An efficient computational procedure to obtain a more stable glass structure, J. Chem. Phys. **151**, 224502 (2019).

[55] F. Lodesani, F. Tavanti, M. C. Menziani, K. Maeda, Y. Takato, S. Urata, and A. Pedone, Exploring the crystallization path of lithium disilicate through metadynamics simulations, Phys. Rev. Mater. **5**, 075602 (2021).

[56] G. E. Jellison, S. A. Feller, and P. J. Bray, A re-examination of the fraction of 4-coordinated boron atoms in the lithium borate glass system, Phys. Chem. Glasses **19**, 52 (1978).

[57] O. L. Alderman, C. J. Benmore, B. Reynolds, B. Royle, S. Feller, and R. J. Weber, Liquid fragility maximum in lithium borate glass-forming melts related to the local structure, Intl. J. Appl. Glass Sci. **14**, 52 (2023).

[58] J. Swenson, L. Börjesson, and W. Howells, Structure of borate glasses from neutron-diffraction experiments, Phys. Rev. B **52**, 9310 (1995).

[59] Y. Onodera, Y. Takimoto, H. Hijiya, T. Taniguchi, S. Urata, S. Inaba, S. Fujita, I. Obayashi, Y. Hiraoka, and S. Kohara, Origin of the mixed alkali effect in silicate glass, NPG Asia Materials **11**, 75 (2019).

[60] J. Swenson, L. Börjesson, and W. Howells, Structure of fast-ion-conducting lithium and sodium borate glasses by neutron diffraction and reverse Monte Carlo simulations, Phys. Rev. B **57**, 13514 (1998).

[61] S. Urata and S. Li, A multiscale shear-transformation-zone (STZ) model and simulation of plasticity in amorphous solids, Acta Mater. **155**, 153 (2018).

[62] C.-T. Yip, M. Isobe, C.-H. Chan, S. Ren, K.-P. Wong, Q. Huo, C.-S. Lee, Y.-H. Tsang, Y. Han, and C.-H. Lam, Direct evidence of void-induced structural relaxations in colloidal glass formers, Phys. Rev. Lett. **125**, 258001 (2020).

[63] B. Kramer and J. Bosman, Open access potential and uptake in the context of Plan S - a partial gap analysis (Version v1), zenodo (2019), https://doi.org/10.5281/zenodo.3549020.